

Surface-wave inversion for a P-velocity profile with a constant depth gradient of the squared slowness

A.V. Ponomarenko^{1*}, B.M. Kashtan¹, V.N. Troyan¹ and W.A. Mulder^{2,3}

¹Saint Petersburg State University, Ulyanovskaya St. 1, 19804 St. Petersburg, Russia, ²Shell Global Solutions International B.V., PO Box 60, 2280 AB Rijswijk, The Netherlands, and ³Faculty of Civil Engineering and Geosciences, Department of Geoscience & Engineering, Delft University of Technology, PO Box 5048, 2600 GA Delft, The Netherlands

Received May 2015, revision accepted July 2016

ABSTRACT

Surface waves are often used to estimate a near-surface shear-velocity profile. The inverse problem is solved for the locally one-dimensional problem of a set of homogeneous horizontal elastic layers. The result is a set of shear velocities, one for each layer. To obtain a P-wave velocity profile, the P-guided waves should be included in the inversion scheme. As an alternative to a multi-layered model, we consider a simple smooth acoustic constant-density velocity model, which has a negative constant vertical depth gradient of the squared P-wave slowness and is bounded by a free surface at the top and a homogeneous half-space at the bottom. The exact solution involves Airy functions and provides an analytical expression for the dispersion equation. If the v_s/v_p ratio is sufficiently small, the dispersion curves can be picked from the seismic data and inverted for the continuous P-wave velocity profile. The potential advantages of our model are its low computational cost and the fact that the result can serve as a smooth starting model for full-waveform inversion. For the latter, a smooth initial model is often preferred over a rough one. We test the inversion approach on synthetic elastic data computed for a single-layer P-wave model and on field data, both with a small v_s/v_p ratio. We find that a single-layer model can recover either the shallow or deeper part of the profile but not both, when compared with the result of a multi-layer inversion that we use as a reference. An extension of our analytic model to two layers above a homogeneous half-space, each with a constant vertical gradient of the squared P-wave slowness and connected in a continuous manner, improves the fit of the picked dispersion curves. The resulting profile resembles a smooth approximation of the multi-layered one but contains, of course, less detail. As it turns out, our method does not degrade as gracefully as, for instance, diving-wave tomography, and we can only hope to fit a subset of the dispersion curves. Therefore, the applicability of the method is limited to cases where the v_s/v_p ratio is small and the profile is sufficiently simple. A further extension of the two-layer model to more layers, each with a constant depth gradient of the squared slowness, might improve the fit of the modal structure but at an increased cost.

Key words: P-wave velocity profile, Squared-slowness gradient, Surface-wave inversion.

*E-mail: andrey.v.ponomarenko@mail.ru

INTRODUCTION

Surface waves are widely used for the characterisation of the near surface. Often, a 1-D model consisting of a sequence of homogeneous horizontal elastic layers is considered, leading to a dispersion equation. The roots of the dispersion equation represent the various modes of the surface waves. The solution of the inverse problem is a set of parameter values that describe the layers in the profile (Socco, Foti, and Boiero 2010). Usually, the shear-wave velocities are reconstructed by inverting the fundamental mode of the Rayleigh wave. This mode and the higher modes, which are also called normal modes, are described by the real roots of the dispersion equation. A P-wave velocity profile can be estimated if P-guided waves are used in the inversion scheme (Boiero, Maraschini, and Socco 2009; Ernst 2013). These waves, which are also known as fast leaking elastic modes, correspond to the complex roots of the dispersion equation (Roth and Holliger 1998; Boiero, Wiarda, and Vermeer 2013; Anikiev *et al.* 2014).

If one wants to invert for a smoothly varying gradient-type near-surface velocity model, e.g., to obtain a smooth starting model for full-waveform inversion, a large number of homogeneous layers with small velocity contrasts between them can, in principle, be considered. In practice, however, a large number of layers increases the calculation time and may cause convergence problems due to an increased number of local minima. A continuous medium may be a useful alternative. We therefore consider a smooth acoustic velocity medium: a layer with a linear decrease in the squared slowness with depth. This means that the vertical gradient of the squared slowness has a constant negative value. The layer is bounded from above by the free surface and from below by a homogeneous acoustic half-space. Three parameters describe the continuous velocity profile: v_0 , the P-wave velocity at the surface; a , the non-negative depth gradient parameter of the squared P-wave slowness; and h , the height or thickness of the layer. The density is assumed to be constant. This medium has an analytical solution for the wavefield (Brekhovskikh 1980). The solution can be expressed in terms of Airy functions and is much simpler than that for a constant acoustic velocity gradient, which requires Bessel functions of imaginary order (Alekseev 1958; Kuvshinov and Mulder 2006; Kazei *et al.* 2013). This allows us to obtain a dispersion equation, similar to the multi-layer case, and invert the dispersion curves to obtain a P-wave velocity profile. We invert the dispersion curves of the normal acoustic modes by direct minimisation of the dispersion equation, as proposed by Ernst

(2007). The extension to a continuous model with multiple layers, each with a constant squared-slowness depth gradient, is straightforward and seems to be a promising tool, but a larger number of parameters will make inversion more difficult. Here, we only consider a two-layer example with five parameters in addition to the one-layer example mentioned before.

To employ an acoustic model for the estimation of a P-wave velocity profile from elastic data, the v_s/v_p ratio in the near surface has to be small, which is often but not always the case. If it is, the P-guided waves can be distinguished from the Rayleigh waves. We can then use the acoustic theory for P-guided waves to approximate the elastic case because of the similarity between normal acoustic modes and fast leaking elastic modes (Roth and Holliger 1998).

In the following section, we present the dispersion equations for our simple models. Then, we describe the inversion approach. To evaluate its potential, we invert the P-guided waves of 2-D synthetic elastic data computed for our P-wave model with one layer over a half-space. We then apply the method to land data and first consider inversion for a single layer with three parameters. Since the result can explain either the shallow or deeper events, but not both at the same time, we also consider inversion for a model with two layers and five parameters and compare the obtained results with that of multi-layered inversion.

THEORY OF THE FORWARD PROBLEM

Single layer above a half-space

We consider a 2-D isotropic acoustic constant-density model with a layer that has a constant depth gradient of the squared slowness on top of a homogeneous half-space. A free-surface boundary condition is included. The velocity in the layer obeys $v_1(z) = v_0/\sqrt{1-az}$. The deeper half-space starts at a depth h and has a constant velocity $v_2 = v_1(h)$, so there is no velocity contrast. The velocity profile exists for values of the gradient parameter a and the depth of the half-space h satisfying $ah < 1$, where a and h are supposed to be positive.

Figure 1 shows the geometry of the model and an example of a velocity profile.

For a medium with constant density and with its properties depending on depth z , the wave equation for the pressure can be written as

$$\nabla \cdot \nabla P(x, z, t) - \frac{1}{v_1^2(z)} \frac{\partial^2 P(x, z, t)}{\partial t^2} = 0, \quad (1)$$

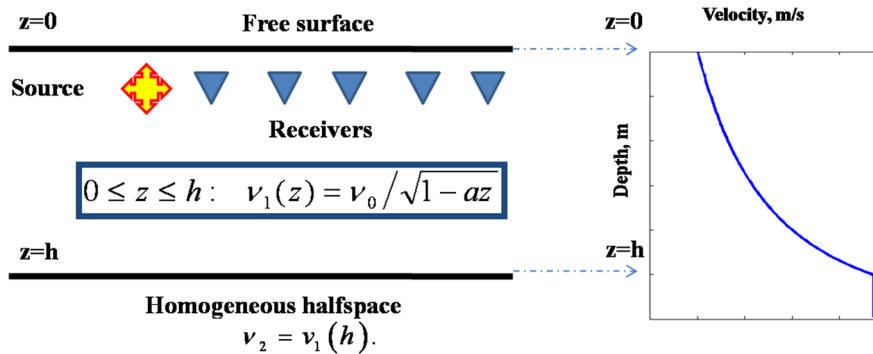


Figure 1 Geometry of the single-layer model with an example of a velocity profile on the right.

with the earlier $v_1(z)$. After a Fourier transform in time and in the horizontal coordinate x , followed by the change of coordinates,

$$\tau = \tau_0 + \frac{z}{H}, \quad \tau_0 = H^2(k^2 - k_0^2), \quad H = (ak_0^2)^{-1/3}, \quad (2)$$

with $k_0 = \omega/v_0$ and $\omega = 2\pi f$ the angular frequency, the wave equation (1) transforms to the classic Airy equation:

$$\frac{\partial^2}{\partial \tau^2} \hat{P}(\tau) - \tau \hat{P}(\tau) = 0, \quad \tau = \tau(z, k, \omega, v_0, a). \quad (3)$$

Details can be found in Appendix A. Equation (3) has two linearly independent solutions, corresponding to the two Airy functions $\text{Ai}(\tau)$ and $\text{Bi}(\tau)$ with real argument τ (for example, see Brekhovskikh 1980). The analytical expression for the wavefield in the layer can be expressed as their linear combination. Together with the free-surface boundary condition of zero pressure and the continuity conditions of pressure and the normal component of the particle velocity at the interface between the layer and the half-space, we obtain the dispersion equation (see Appendix A):

$$\begin{aligned} \mathcal{D} = & \text{Ai}(\tau)|_{z=0} \{ \text{Bi}'(\tau)|_{z=h} + H\alpha_2 \text{Bi}(\tau)|_{z=h} \} \\ & - \text{Bi}(\tau)|_{z=0} \{ \text{Ai}'(\tau)|_{z=h} + H\alpha_2 \text{Ai}(\tau)|_{z=h} \} = 0, \end{aligned} \quad (4)$$

where $\alpha_2 = \sqrt{k^2 - (\omega/v_2)^2}$. The primes denote the derivatives with respect to τ . The roots of this equation are the functions $k(\omega)$. They allow us to evaluate the dispersive phase velocities $V(\omega) = \omega/k(\omega)$ of the interference guided acoustic modes.

The left-hand side of the dispersion equation (4), which we refer to as the dispersion expression, can become complex if the factor α_2 becomes complex, which happens if the phase velocity V exceeds v_2 . The dispersion expression equals zero in the range of frequencies for which the phase velocity is real and obeys $v_0 \leq V \leq v_2$.

The dependence of the wavenumbers or phase velocities on the angular frequency ω is usually presented as a dispersion

curve. To obtain the dispersion curve, we used the bisection method to find the real roots of the dispersion equation. As an example, Fig. 2 depicts the dispersion curves of the phase velocity values for normal acoustic modes. They are shown for the frequency interval from 0 to 100 Hz, using the velocity parameters $v_0 = 1.5$ km/s, $h = 100$ m, $a = 8 \cdot 10^{-3} \text{m}^{-1}$ — the same parameters as in the synthetic example to be discussed later on. With increasing frequency, the number of roots also increases, leading to an increase in the number of curves in Fig. 2. Similar as that with Rayleigh waves, these dispersion curves can be inverted to estimate the model parameters.

Two layers above a half-space

We also consider the extension of the model to two layers above a constant half-space, where each of the layers has a constant depth gradient of the squared slowness. Again, a free-surface boundary condition is imposed. The velocity in the

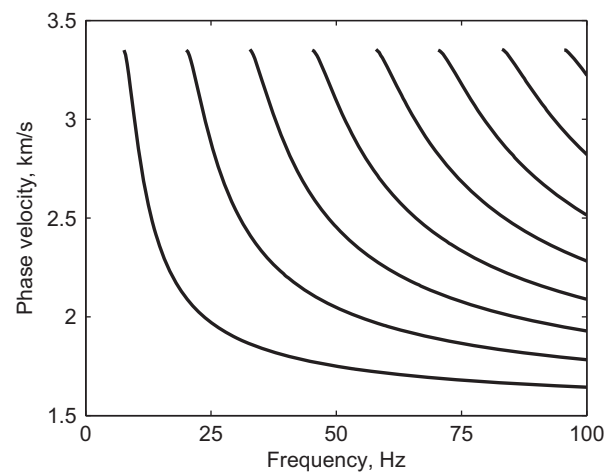


Figure 2 Dispersion curves of the phase velocities for the normal acoustic modes in a single-layer model.

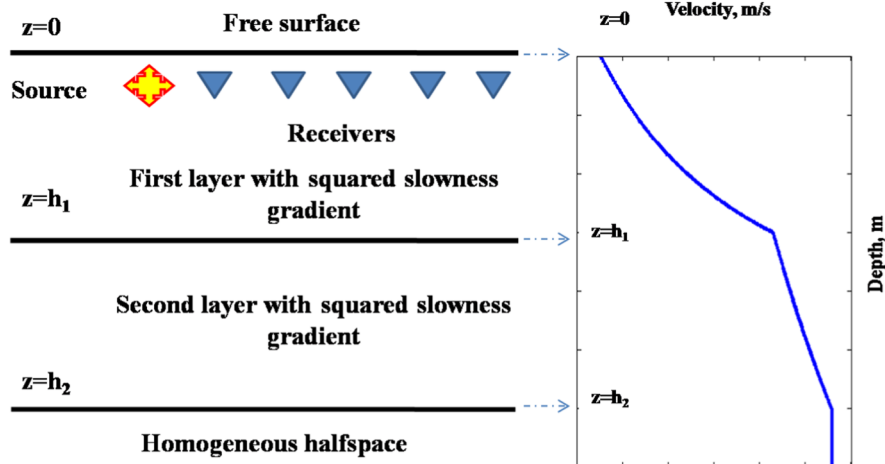


Figure 3 Geometry of the two-layer model with an example of a velocity profile on the right.

first layer is given by $v_1(z) = v_0/\sqrt{1 - a_1 z}$ and in the second layer by $v_2(z) = v_1(h_1)/\sqrt{1 - a_2(z - h_1)}$. The half-space below starts at a depth h_2 and has a constant velocity $v_3 = v_2(h_2)$, so again, there are no velocity contrasts. Also, we again assume the density to be constant in the whole model, for simplicity. The velocity profile exists for positive $a_1, h_1, a_2,$ and h_2 values satisfying $a_1 h_1 < 1$ and $a_2(h_2 - h_1) < 1$. The geometry of the model and an example of a velocity profile are sketched in Fig. 3. Five parameters, instead of three, describe the model. Similar to the single-layer model, we can derive the dispersion equation (see Appendix B) and invert the dispersion curves to estimate the model parameters.

As an example, the dispersion curves of the phase velocities for the normal acoustic modes are shown in Fig. 4, where all real roots of the corresponding dispersion equation are

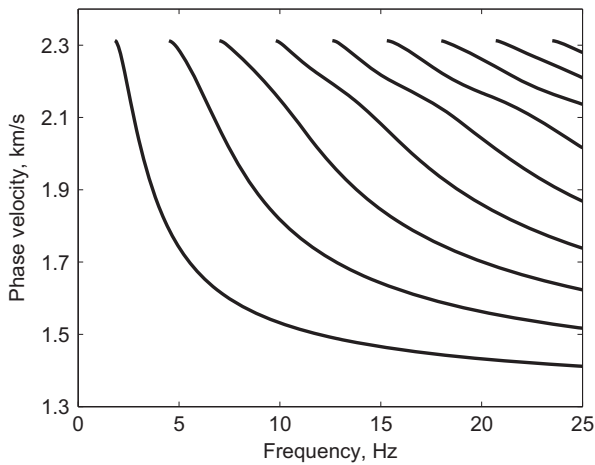


Figure 4 Dispersion curves of the phase velocities for the normal acoustic modes in a two-layer model.

displayed for the frequency interval between 0 and 25 Hz, using the velocity parameters $v_0 = 1.3$ km/s, $h_1 = 300$ m, $a_1 = 2 \cdot 10^{-3} \text{ m}^{-1}$, $h_2 = 600$ m, and $a_2 = 0.7 \cdot 10^{-3} \text{ m}^{-1}$.

Inversion

To solve the inverse problem, we choose a misfit functional of the following form:

$$F_j(\mathbf{p}) = \sqrt{\sum_i \mathcal{D}_{ij}^2(f_{ij}, V_{ij}, \mathbf{p})}, \tag{5}$$

where \mathcal{D}_{ij} is the value of the dispersion expression, computed for a frequency f_{ij} and phase velocity V_{ij} . The index i denotes a point on the dispersion curve, whereas j is the number of the picked dispersion curve or mode. Note that, for the single-layer model, $\mathbf{p} = (v_0, a, b)$ and, for the two-layer model, $\mathbf{p} = (v_0, a_1, h_1, a_2, h_2)$. A misfit functional of this form allows for direct minimization without including a root search in the inversion process and, more importantly, is independent of any errors related to the misidentification of modes (Ernst 2007; Maraschini et al. 2010).

Synthetic Example

We created a synthetic test example for a single-layer model with the aid of the 2-D isotropic elastic modelling code REM2D from Hamburg University (Kosloff et al. 1989; Tessmer 2011). Figure 1 shows the geometry of the model. Its parameters are the P-wave and S-wave velocities at the surface ($v_{p,0} = 1.5$ km/s and $v_{s,0} = 0.5$ km/s, respectively) the density at the surface (2200 kg/m^3), and a gradient parameter in the layer ($a = 8 \cdot 10^{-3} \text{ m}^{-1}$), which is taken to be the same for

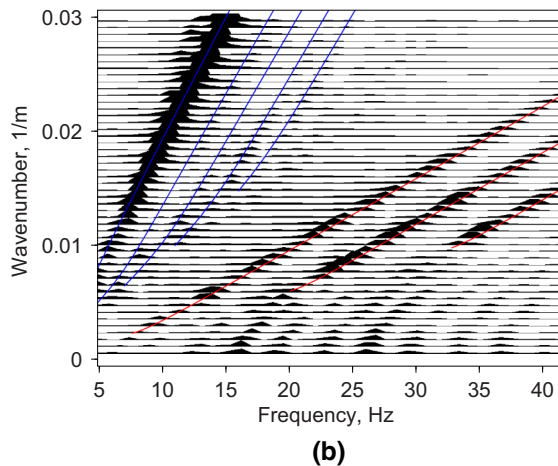
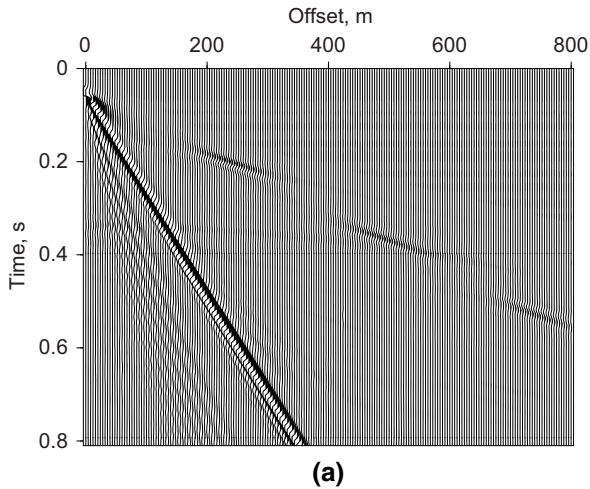


Figure 5 Synthetic pressure seismogram in the (a) x, t and (b) f, k domains for a vertical-force source. The early arrivals in (a) are the P-guided waves, and the estimated dispersion curves are drawn in red in (b). The blue lines in (b) correspond to the Rayleigh waves, which appear as the later and stronger events in (a). They are not considered in the inversion.

v_p^{-2} , v_s^{-2} , and ρ^{-2} . In this case, we let the density vary with depth to obtain a closer resemblance to the field observations. The homogeneous half-space starts at a depth $h = 100$ m. A point source with a central frequency of 20 Hz is placed at a depth of 4 m below the free surface. The receivers are buried at the same depth. We consider a vertical-force source and record the pressure. The resulting seismograms in the x, t and f, k domains are shown in Fig. 5(a) and (b), respectively. Because of the small v_s/v_p ratio, the P-guided waves can be clearly distinguished from the Rayleigh waves. In Fig. 5(b), two sets of spectral maxima appear. One set consists of the Rayleigh waves. Their dispersion curves are marked by blue

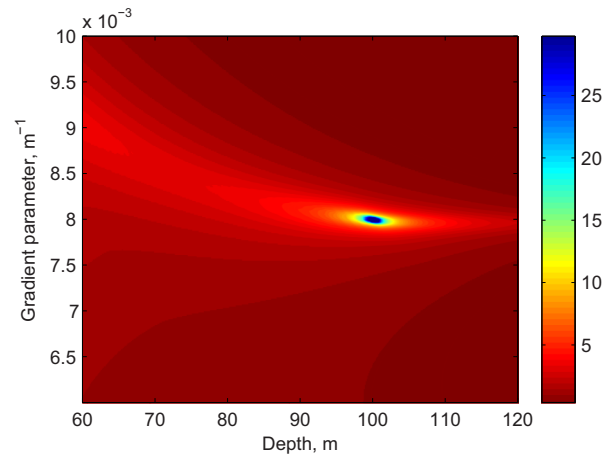


Figure 6 Inverse of the misfit functional at the true value of v_0 as function of depth h and gradient parameter a .

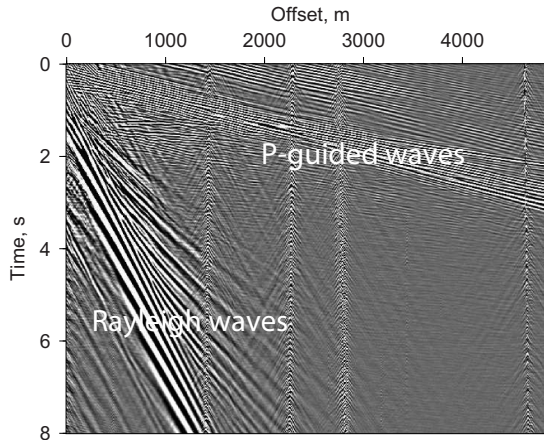
lines. The other set of spectral maxima consist of P-guided waves. Their dispersion curves can be estimated by the roots of the dispersion equation (4), drawn in red, and contain information about the P-wave velocity in the model. The upper curve from this set starts at a frequency of 7.48 Hz. This is the lowest frequency for which the roots of the dispersion equation lie on the real axis of the complex plane (k, ω).

We earlier examined this synthetic example (Ponorenko *et al.* 2013), considering a one-parametric Newton inversion to minimise the functional (5) for the gradient parameter a , assuming that we knew the true values of v_0 and h . We used the known dispersion curves of the three dispersive modes as input data and found that the inversion can give us the proper gradient value over a wide range of velocity models.

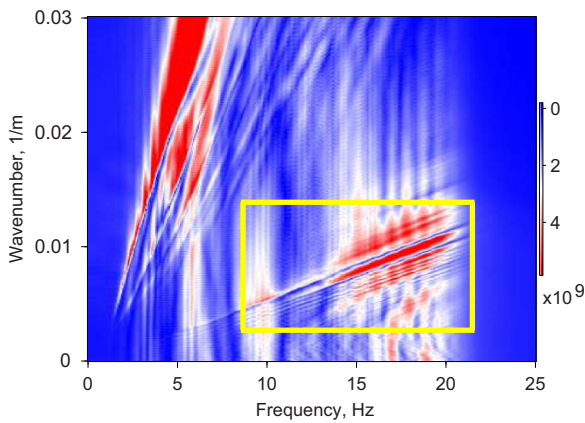
Here, we apply a three-parameter direct grid search over the surface velocity v_0 , gradient a , and thickness h to find the global minimum of the misfit functional for the first dispersive mode at frequencies below 20 Hz. In Fig. 6, the inverse of the misfit functional is shown at the true $v_0 = v_{p,0} = 1.5$ km/s as a function of depth h and gradient parameter a . Values above 30 were clipped, and values for $ah > 1$ were obtained by constant extrapolation from nearby. The inverse functional has a sharp global maximum at the true solution $a = 8 \cdot 10^{-3} \text{ m}^{-1}$ and $h = 100$ m. This suggests that the method may also work on real data with a small v_s/v_p ratio.

Real data

We apply the method to the pre-processed vibroseis data shown in Fig. 7(a). This seismogram represents the vertical



(a)



(b)

Figure 7 Real-data seismogram with the vertical particle velocity in the (a) x, t and (b) f, k domains. The yellow box for the latter contains the P-guided waves.

particle velocity. It is clear from the seismogram that the v_s/v_p ratio is small and the P-guided waves can be easily distinguished from the Rayleigh waves. In the f, k domain, shown in Fig. 7(b), two types of waves appear as two sets of spectral maxima. The set with smaller wavenumbers and higher frequencies corresponds to the P-guided waves, contained inside the yellow box in Figure 7(b), whereas the set with higher wavenumbers corresponds to the Rayleigh waves or ground roll. Note that the same distinction is made in Fig. 5(b) for the synthetic data. With the real data, we again focus on the spectral maxima of the P-guided waves to estimate the P-wave velocity profile.

We pick the main dispersion events as straight lines from the yellow box in Fig. 7(b). We trace them starting from a reference points of high amplitude for selected events in the

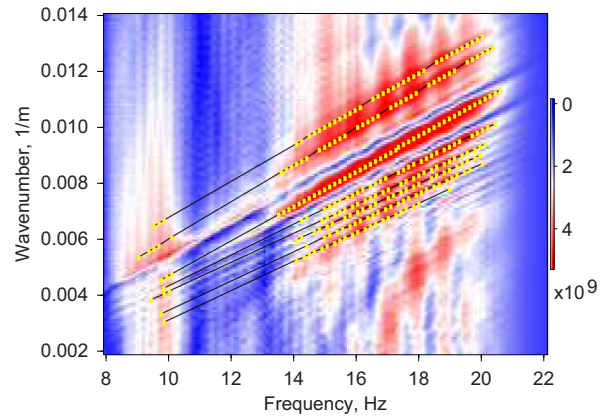


Figure 8 Maxima of the real-data seismogram in the f, k -domain (red) and picked events (black lines, yellow dots). The domain corresponds to the yellow box in Fig. 7(b). We number the dispersion curves from 1 to 8, starting at the highest wavenumber and moving down.

amplitude-clipped f, k spectrum. The resulting picked events are drawn in Fig. 8. There are eight curves, counting from the high to the low wavenumbers. We skip the stretched event between the second and third curves because it has a much lower amplitude than the neighbouring curves for frequencies between 14 and 20 Hz, where most of the picked points reside. Note that the slopes of the first three lines are larger than those of the other five.

Heuristic approach

To obtain some insight into the qualitative behaviour of dispersion curves of a single-layer model for different parameters, we compute dispersion curves for several choices of v_0, h , and a . Table 1 lists four of them. The corresponding curves are displayed in Fig. 9. We observe, first, that a smaller value of v_0 leads to a shift of the dispersion curves towards the larger wavenumbers. Secondly, a decrease in h , together with an increase in a , causes the modal number to decrease and, at

Table 1 The four sets of parameters used to gain some insight into the qualitative behaviour of the dispersion curves

	v_0 (km/s)	h (m)	a (m^{-1})
(a)	1.41	700	$0.85 \cdot 10^{-3}$
(b)	1.50	600	$1.00 \cdot 10^{-3}$
(c)	1.45	500	$1.50 \cdot 10^{-3}$
(d)	1.65	400	$1.85 \cdot 10^{-3}$

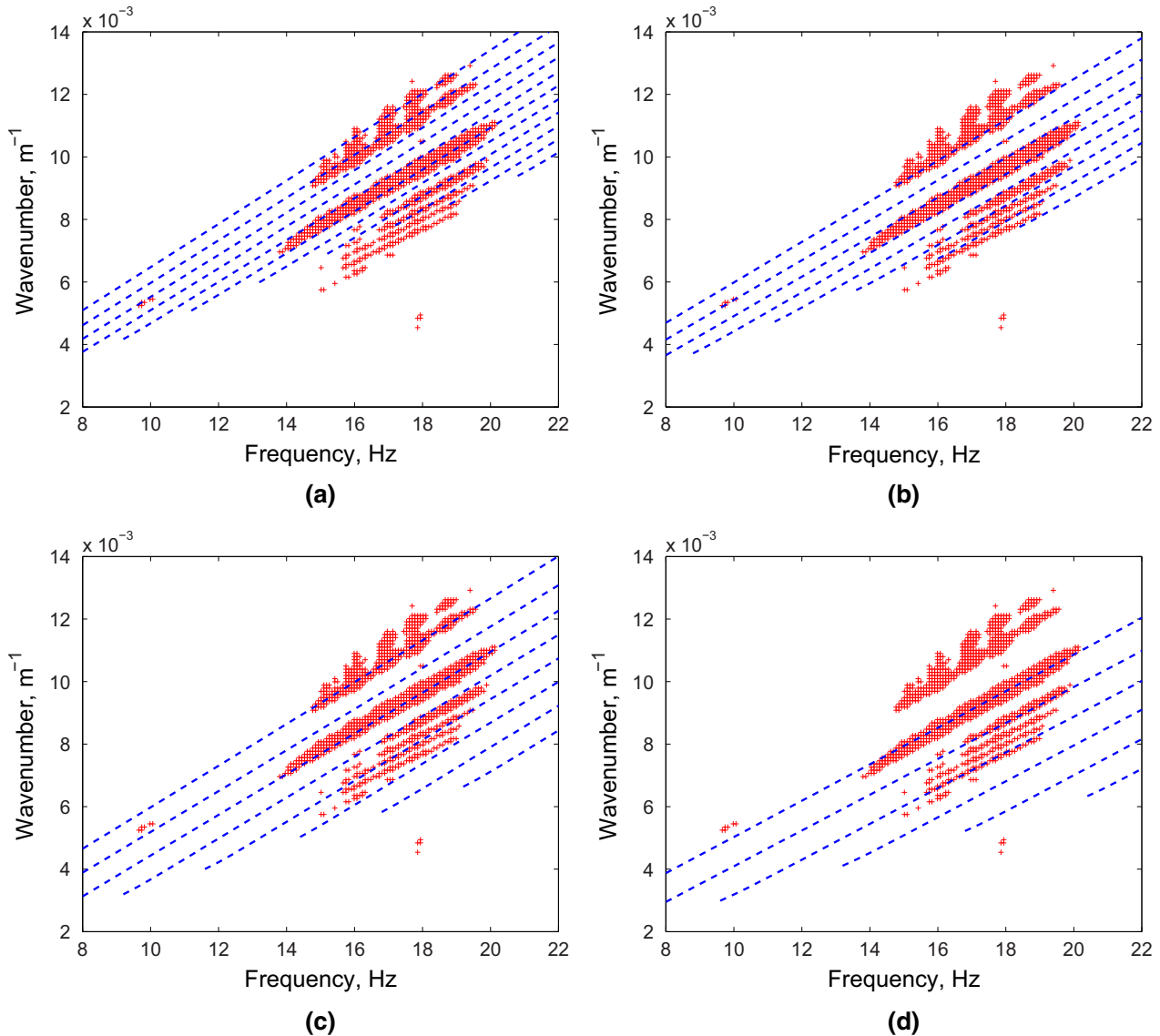


Figure 9 Maxima of the real-data seismogram in the f, k domain from Fig. 8 (red crosses) with dispersion curves (blue) for a single-layer model. The sets of the model parameters v_0 , b , and a for each panel are listed in Table 1. This illustrates the qualitative behaviour of the dispersion curves when the parameters are changed.

the same time, increases the distance between the dispersion curves of these modes.

Given these findings and upon closer inspection of the picked events shown in Fig. 8, there appear to be two sets of dispersion curves. Each can be explained by a different set of parameters. We refer to one set, corresponding to the higher wavenumbers or shorter wavelengths, as the “high” modes. It comprises modes 1, 2, and 3, counting from the highest to the lowest wavenumbers. The other set contains the “low” modes, numbered from 4 to 8. They have a smaller slope.

Mode 3 corresponds to a broad and pronounced dispersion event that might also be classified as a low mode. The low modes “see” a deeper part of the model and correspond to higher velocities than the high modes. The analytical model may better explain the dispersion curves if we would fit each set of modes with each own set of parameters.

Given these heuristics, we search for a set of parameters by scanning through (v_0, b) pairs followed by a one-parameter search for a , independently for the low and high modes. For the high modes, we find that $v_0 = 1.35$ km/s, $b = 350$ m and

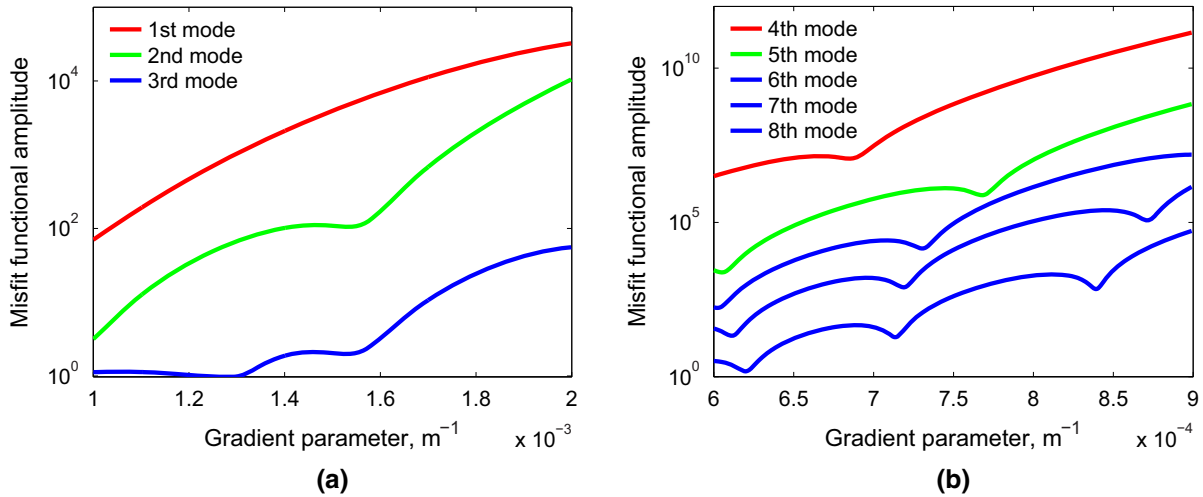


Figure 10 Misfit functionals for (a) the high modes at fixed parameters $v_0 = 1.35$ km/s and $b = 350$ m and for (b) the low modes with $v_0 = 1.75$ km/s and $b = 950$ m. There are several local minima, and the best fit is obtained where these more or less coincide.

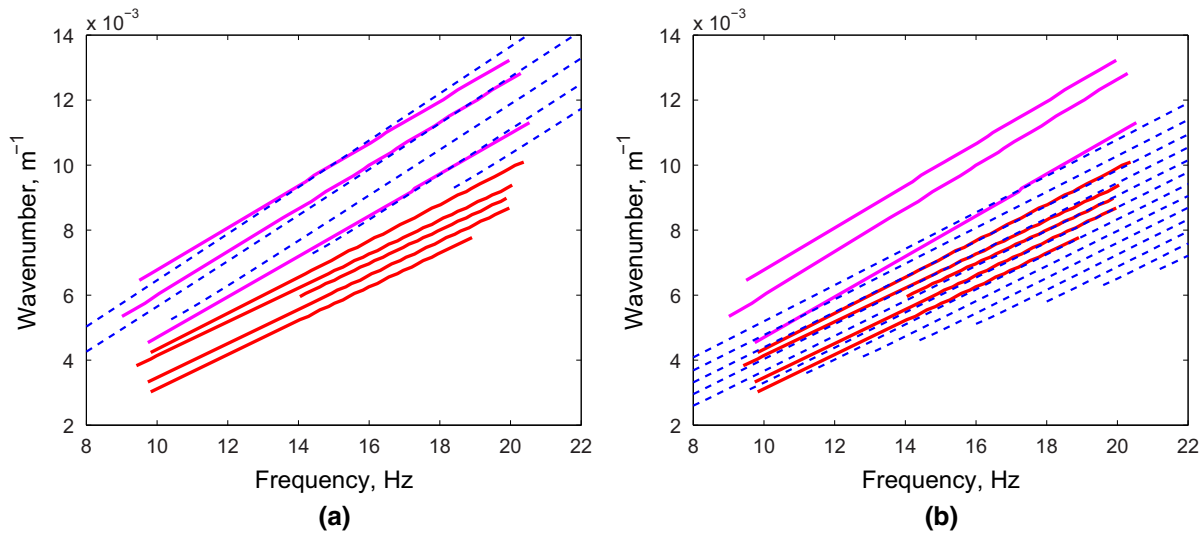


Figure 11 Predicted modal structure (blue) for the high (a) and low modes (b), obtained with the heuristic approach, together with the picked events from Figure 8 (high modes are in magenta, low are in red).

$a = 1.53 \cdot 10^{-3} \text{ m}^{-1}$ provide a reasonable data fit, whereas for the low modes, we obtain $v_0 = 1.75$ km/s, $b = 950$ m and $a = 0.723 \cdot 10^{-3} \text{ m}^{-1}$.

Figure 10 shows the misfit functionals for the high modes and the low modes, respectively, as a function of the gradient parameter a , each for the aforementioned choices of v_0 and b . Several local minima show up in this one-parameter cross section of the functionals. For the low modes in Fig. 10(b), the local minima are sharper and closer to each other at the value of $a = 0.723 \cdot 10^{-3} \text{ m}^{-1}$ found by the one-parameter search, which is not true for other values of a and for other scanned pairs of (v_0, b) . A similar but less pronounced behaviour is

observed for the two high modes in Fig. 10(a), and we find the same value of $a = 1.53 \cdot 10^{-3} \text{ m}^{-1}$ as for the low modes. Figure 11 shows a set of dispersion curves for the aforementioned set of parameters for the (a) high and (b) low modes, together with the picked events in the f, k domain. Note that more modes are drawn than were picked and not all modes coincide with maxima in the seismogram, indicating that the implemented approach does not lead to a model that can accurately explain the data. In Fig. 12, we compare the obtained velocity profiles to the result of a multi-layered inversion. The result for the high modes (green) resembles the shallow part of the multi-layered model (red), whereas the profile for the

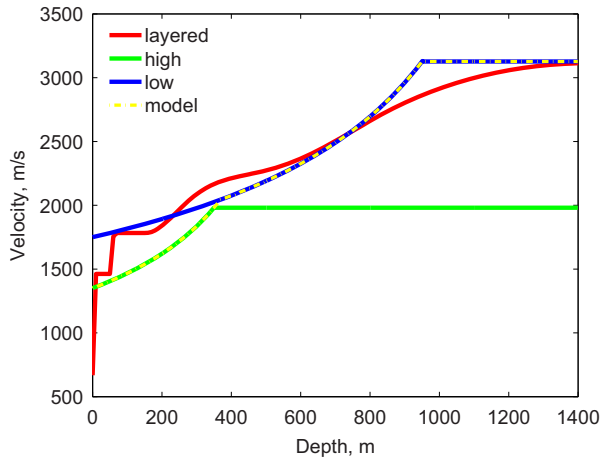


Figure 12 Estimated v_p velocity profiles obtained separately for the high modes (green) and low modes (blue), together with the multi-layer inverted profile (red) shown as a reference. The result for the high modes is closer to the multi-layer profile in the shallow part and that for the low modes in the deeper part. These result suggest that a two-layer gradient model (yellow) may lead to a better data fit.

low modes (blue) more or less follows the deeper part of the multi-layered model. These two velocity profiles seem to provide a reasonable, although not so detailed, approximation of the multi-layered model. This suggests that a two-layer gradient model might do better than two single-layer models, as sketched in Fig. 12 with the yellow curve. Next, we will investigate a single-layer model and then a two-layer model, applying a direct grid search for the global minimum of the misfit functional.

Direct grid search: single layer above a half-space

If the model has a small number of parameters, we can use a direct grid search to solve the inverse problem. For our single-layer model with a linear decrease in the squared slowness, we apply a three-parameter direct grid search to both sets of picked events, using the same misfit functional (5) as before. For the high modes, except the first one, we scan the following parameter ranges: v_0 between 1.1 and 1.5 km/s, h from 0.05 to 0.45 km, and a between 0.9 and 2.6 km^{-1} . For the low modes, we consider v_0 between 1.5 and 2.1 km/s, h from 0.3 to 1.2 km, and a between 0.2 and 1.2 km^{-1} . The increments are chosen to be 50 m/s for the velocity, 4 m for the thickness of the layer, and 0.01 km^{-1} for the gradient parameter. We choose the increments and ranges of the parameters on the basis of some initial tests and results of the earlier qualitative findings. The only reason for

dropping the first high mode (mode 1) is an improvement of the results.

Once the global minimum on the each grid has been found, we start a new search on a finer subset of the initial grid, with an increment of 20 m/s for the velocity but with the same intervals for the other parameters. The resulting parameters for the high modes are $v_0 = 1.42$ km/s, $h = 0.118$ km, and $a = 2.1$ km^{-1} . For the low modes, we found $v_0 = 1.68$ km/s, $h = 0.4$ km, and $a = 0.98$ km^{-1} . Fig. 13(a) and (b) show the 2-D cross sections through the resulting v_0 parameters of the inverse misfit functional for the high and low modes, respectively. The functional for the low modes appears to have several local minima, similar to those shown in Fig. 10(b). These minima appear as local maxima in Fig. 13(b). Their large number justifies the use of the direct grid search for finding the global one.

Figure 14 shows the predicted modal structure for the estimated parameters for the high and low modes together with the picked events. It does not show first the highest mode because that one was ignored during the inversion. Only the upper curves of each set are captured: the green curve and the upper curve of the high picked modes used in the inversion and the third predicted blue curve and the upper curve of the low picked modes. The reason is that the functional (5) is the sum of the functionals for each mode and the functionals at higher wavenumbers have larger amplitudes. This results in a more accurate fit for these modes than for those at lower wavenumbers.

Figure 15 displays the v_p velocity profiles for the estimated parameters from the direct grid search, for each of the two sets. Compared with the multi-layer inversion, the depth of the half-space is underestimated but the velocity trend, described by v_0 and a , agrees with the upper part of the multi-layered profile. This again suggests that a better fit may be obtained by considering two layers above a half-space instead of one, which we will investigate next.

Direct grid search: two layers above a half-space

Since the single-layer model does not provide accurate results, we consider the inversion for a two-layer model with a linear decrease in squared slowness in each layer, bounded from below by a homogeneous half-space. This model might be able to capture both parts of the profile, corresponding to the high and low modes examined before. We apply a five parameter direct grid search using the same misfit functional (5).

First, we scan the following parameter ranges, motivated by those used for the single-layer inversion: v_0 between

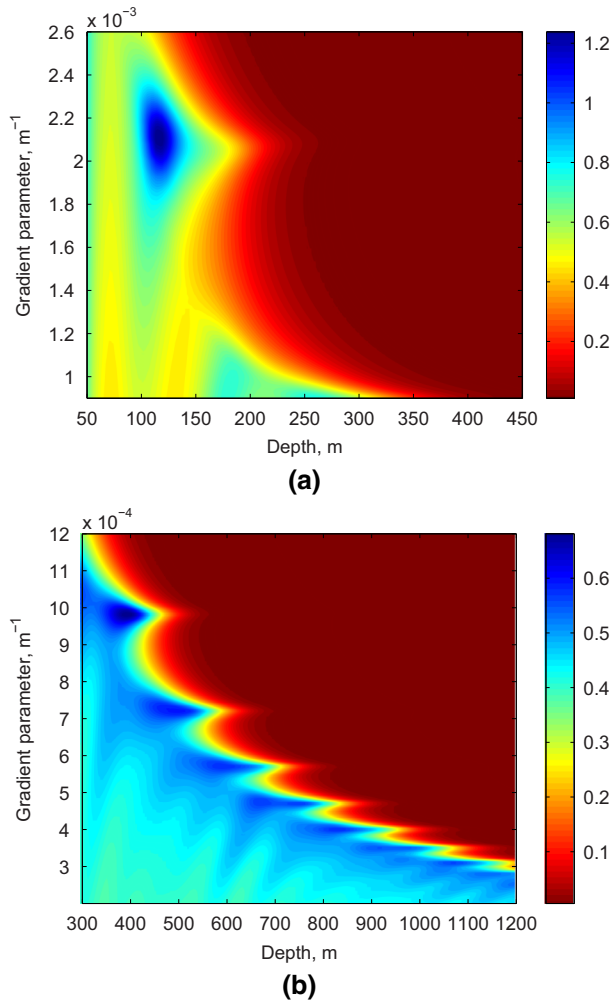


Figure 13 Two-dimensional cross sections of the inverse misfit functionals, which depends on three parameters, obtained for the (a) high and (b) low picked events for a single-layer model. The third parameter is set to the optimal result of the direct grid search: (a) $v_0 = 1.42$ km/s or (b) $v_0 = 1.68$ km/s. In each panel, the blue peak corresponds to the optimum: $h = 0.118$ km and $a = 2.1$ km⁻¹ at (a), and $h = 0.4$ km and $a = 0.98$ km⁻¹ at (b).

1.3 and 1.6 km/s, h_1 from 0.05 to 0.4 km, a_1 between 1.2 and 2.4 km⁻¹, h_2 from 0.4 to 1.0 km, and a_2 between 0.5 and 1.0 km⁻¹. The increments are chosen to be 20 m/s for the velocity, 10 m for the thickness of the top layer, 50 m for the thickness of the bottom layer, and 0.02 km⁻¹ for both gradient parameters.

Simultaneous inversion of the high modes, excluding the first highest mode as well as the low modes, produces the following parameters: $v_0 = 1.42$ km/s, $h_1 = 0.09$ km, $a_1 = 2.2$ km⁻¹, $h_2 = 0.6$ km, and $a_2 = 0.84$ km⁻¹. Figure 16 shows the predicted modal structure for these parameters (predicted

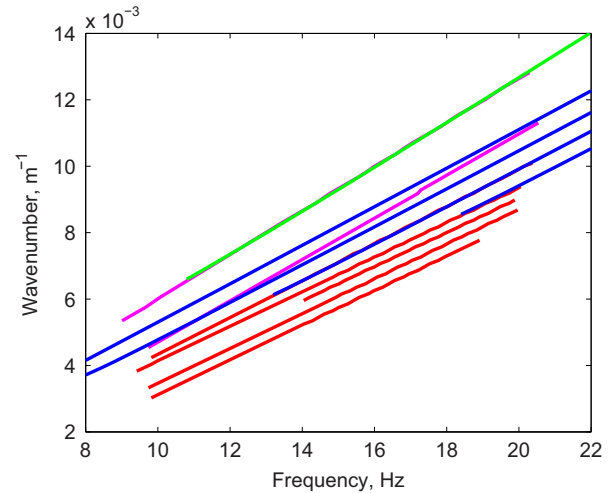


Figure 14 Predicted modal structure for the parameters estimated by the direct grid search with a single-layer model for the high (green) and low (blue) modes. The picked events are shown in magenta (high modes) and red (low modes). The first highest mode has been ignored.

curves in blue, picked events in magenta and red). The green curve in Fig. 19 (“high and low” labels) displays the v_p velocity profile, together with the result of the multi-layer inversion. The predicted modal structure captures only the upper curves (high modes), resulting in a large discrepancy with the multi-layer estimate, except if close the surface.

To capture as many curves as possible, we simultaneously invert only the low modes inside the frequency band from 14 to 20 Hz, where most of the picked events reside.

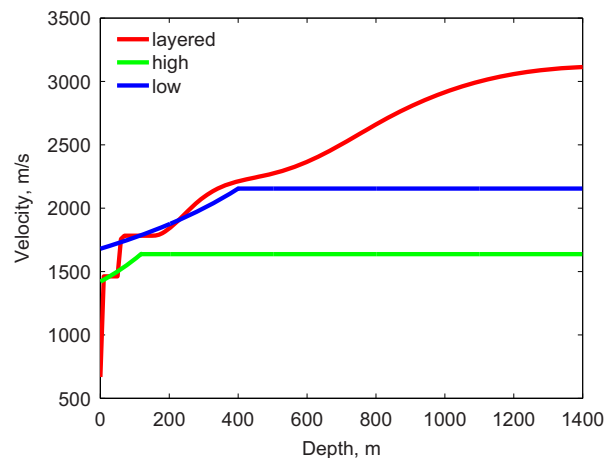


Figure 15 Estimated v_p velocity profiles using the direct grid search on the single-layer model for the high (green) and low (blue) modes, together with the multi-layer inverted profile (red) shown as a reference.

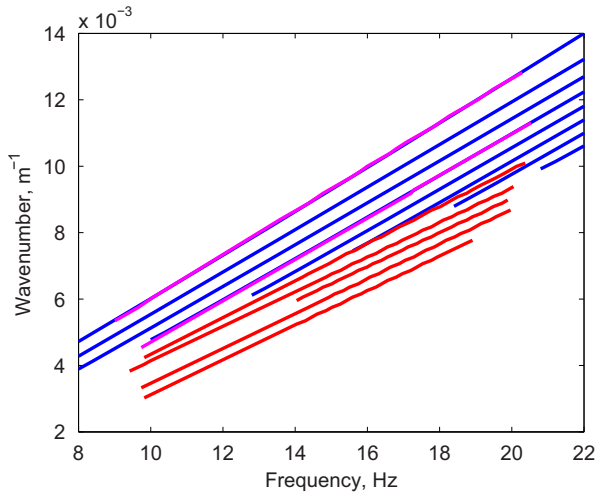


Figure 16 Predicted modal structure (blue) for the parameters estimated by inversion with a two-layer model of both high and low modes. The picked events are shown in magenta (high modes) and red (low modes). The first highest mode has been ignored.

We scan broader intervals: v_0 between 1.3 and 1.8 km/s, h_1 from 0.05 to 0.4 km, a_1 between 1 and 3 km⁻¹, h_2 from 0.4 to 1.0 km, and a_2 between 0.5 and 1.5 km⁻¹. This leads to $v_0 = 1.7$ km/s, $h_1 = 0.06$ km, $a_1 = 2.2$ km⁻¹, $h_2 = 0.9$ km, and $a_2 = 0.68$ km⁻¹. Figure 17 shows the predicted modal structure for these estimated parameters. The corresponding velocity profile is shown in Fig. 19 as a magenta curve (“low1”

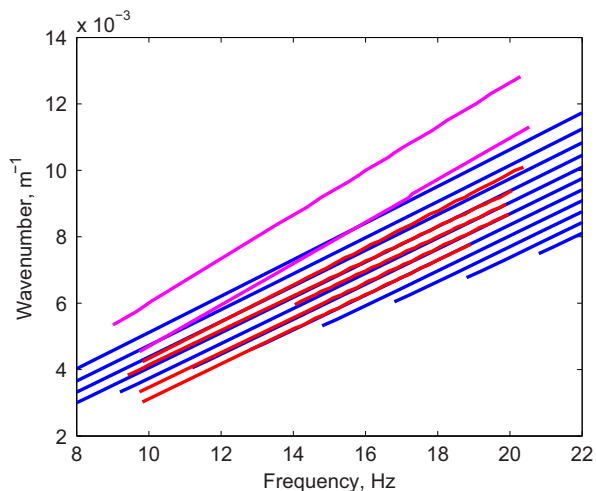


Figure 17 Predicted modal structure (blue) for the parameters estimated by inversion with a two-layer model of only the low modes. The picked events are shown in magenta (high modes) and red (low modes). The first highest mode has been ignored. The slopes now match for the low events but are wrong for the high-wavenumber modes.

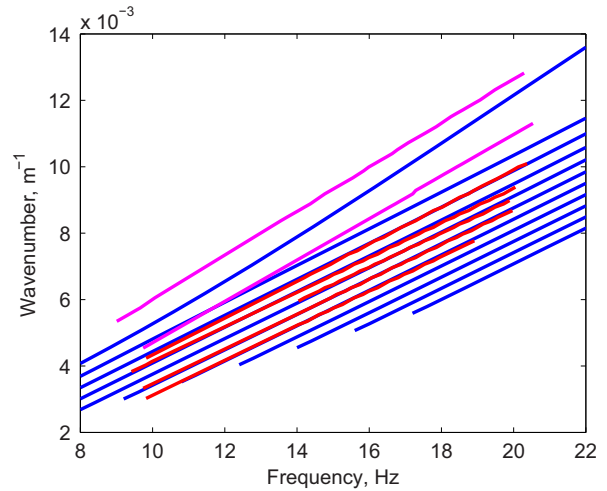


Figure 18 Predicted modal structure (blue) for the parameters estimated with a two-layer model using only the low modes with refined parameter ranges. The picked events are shown in magenta (high modes) and red (low modes). The first highest mode has been ignored.

label). The predicted modal structure here captures the low modes, and the resulting velocity matches most of the multi-layer profile with a slight underestimation of the depth of the half-space. The shallow part of the profile again is different, which suggests that we should search for lower velocities and larger values of the gradient parameter in the first layer.

We therefore modify the parameter ranges, especially for v_0 and a_1 , and take v_0 between 1.1 and 1.4 km/s, h_1 from 0.05 to 0.4 km, a_1 between 5 and 8 km⁻¹, h_2 from 0.5 to 1.2 km, and a_2 between 0.5 and 1 km⁻¹. We use the same increments as before and only change the one for the first gradient parameter a_1 to 0.1 km⁻¹. This produces $v_0 = 1.3$ km/s, $h_1 = 0.08$ km, $a_1 = 6.3$ km⁻¹, $h_2 = 1.0$ km, and $a_2 = 0.7$ km⁻¹. Figure 18 shows the predicted modal structure for the estimated parameters, and the blue curve in Fig. 19 (“low2” label) depicts the v_p velocity profile. The predicted modal structure again captures the low modes, but a smaller velocity value, together with a larger value of the first gradient, leads to a better agreement with a larger part of the multi-layer profile.

DISCUSSION

We attempted to explain field data with dispersion equations for a simple P-wave velocity profiles with a constant depth gradient of the squared P-wave slowness. For the inversion, we first took a heuristic approach with a single-layer model

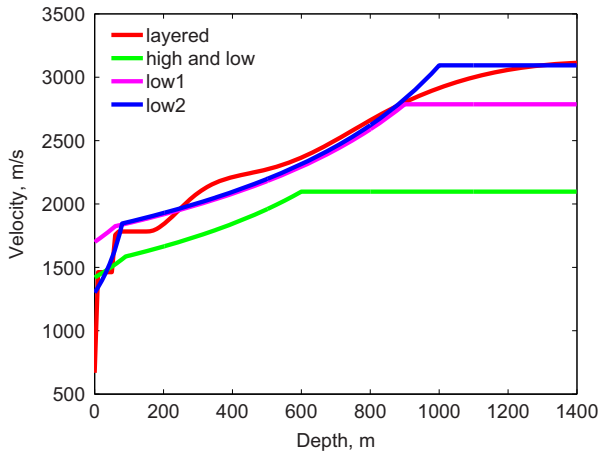


Figure 19 Estimated v_p velocity profiles using a direct grid search for the two-layer model (see labels and descriptions in the text), together with the multi-layer inverted profile (red) shown as a reference.

by analysing dispersion curves for several sets of parameters v_0 , h , and a . This offered some insight into how the dispersion curves depend on the parameters and revealed that the model is too simple to explain the field data, because not all curves can be modelled when trying to fit a simpler model to the data. Then, we divided the modes from the picked events into two subsets: the “high” and “low” modes. Each subset appeared to be reasonably well explained by its own triple of parameters. The high modes have larger wavenumbers and shorter wavelengths and are mainly sensitive to the shallower part. The low modes have longer wavelengths and have seen the deeper parts of the velocity profile. We analysed each set separately by scanning through the surface velocity v_0 and top layer depth h , followed by a one-parameter search over a range of values for the gradient of the squared slowness. Then, we applied a direct grid search to find the best parameters for each set of modes. The results obtained by both methods are quite different. The estimated parameters for each of the modal sets obtained by the heuristic approach predict additional dispersion curves that are absent from the data (Fig. 11). In contrast, the dispersion curves obtained by the direct grid search miss some of the curves in the data (Fig. 14). The velocity profiles estimated with the heuristic approach (Fig. 12) generally approximate the multi-layer profile, but of course without its details. The velocity profiles after the direct grid search more or less approximate only the shallow part of the multi-layer velocity profile (Fig. 15). All this reflects that such a simple single-layer model cannot fully explain the data.

We therefore introduced a two-layer model to allow for a better data fit than with the single-layer model above a

half-space. The inversion of both high and low modes simultaneously failed to provide an estimate that resembled the reference profile of the multi-layer inversion. However, inversion of only the low modes produced a better result in terms of both the predicted modal structure (Fig. 18) and the estimated velocity profile (Fig. 19). The latter provides a reasonable piecewise smooth approximation that resembles the multi-layer inversion result used as a reference. This smooth approximation can be useful as an alternative for a smoothed multi-layer model and might be more appropriate as a starting model for acoustic full-waveform inversion. The predicted modal structure still contains additional dispersion curves that are absent from the data, but the other curves coincide well with the corresponding picked events.

At this point, we have to conclude that our method does not degrade as gracefully as, for instance, diving-wave tomography (Pratt *et al.* 1996; Ravaut *et al.* 2004). For the latter, a simplified smooth subsurface model may still provide a fairly accurate data fit, particularly at the lower frequencies. In our case, a model with less detail misses some of the dispersion curves and, at the same time, predicts additional curves where these are not any observed. This implies that the method is quite sensitive to the details of the subsurface. While this sensitivity can be exploited to provide information about complex subsurface structures, it will make inversion less easy.

An extension of the two-layer model to many layers, each with a constant depth gradient of the squared slowness, might further improve the fit of the modal structure, especially for the media with complex structures. It would, however, increase the number of parameters and computational cost. Then, one might as well use the more powerful approach proposed by Ernst (2013). The computational cost can be lowered by choosing a more powerful global optimisation algorithm than a direct grid search. The main reason for using the latter is that it allowed us to examine cross sections of the misfit functionals.

CONCLUSION

We have applied surface-wave inversion on picked dispersion curves for P-guided waves to estimate a simple continuous P-wave velocity profile from elastic data with a small v_s/v_p ratio. We first considered a profile consisting of a layer with a constant depth gradient of the squared slowness on top of a homogeneous half-space. The model has three parameters, the velocity at the surface, the gradient, and the

thickness of the layer. The second profile consisted of two layers, each with a constant depth gradient of the squared slowness, on top of a half-space with a constant velocity and had five parameters: the velocity at the surface, two gradients, and two thicknesses. The inversion required picking of the P-guided wave dispersion curves, which was carried out in the f, k domain. Model parameters were found by minimisation of a functional by means of a direct grid search for both the single- and two-layer profiles. We found that the single-layer model was not able to properly explain the dispersion curves of a field dataset. Parameter fits for the individual curves suggested the presence of two sets of curves that could be explained by two set of parameters: one for the shallow part of the model and one for the deeper parts. The two-layer model better explained the observed set of lower dispersion curves and finally led a reasonable estimation of the velocity profile, compared with the result of a multi-layer inversion, but not with as much detail since our model only has five parameters to explain the multi-modal structure of the data. Better fits can presumably be obtained by increasing the number of layers, each having a constant depth gradient of the squared slowness. This should be relatively straightforward to implement.

Our results show that the method can provide a piecewise smooth approximation of the P-wave velocity profile for a medium with a small v_s/v_p ratio and a non-trivial but not too complex subsurface structure. For such media, our method may be faster than existing inversion methods that determine piecewise constant velocities. A disadvantage of our approach is the required picking of the P-guided wave dispersion curves and its inability to fit all the picked events. An advantage is its simplicity and its ability to provide smooth models that can directly serve as a starting model for acoustic full-waveform inversion.

ACKNOWLEDGEMENTS

The authors express their gratitude to Ekkehart Tessmer from the Institute of Geophysics, University of Hamburg, for allowing the use of his REM2D code to generate the synthetic seismograms. We also thank Fabian Ernst for the helpful discussions and for providing the multi-layer profile reconstructed from the land data.

This work was supported by Shell Global Solutions International BV under CRDF grant RUG1-30020-ST-11. Additional support was provided by Saint-Petersburg State University under research grant 11.38.217.2014. The Computer Centre of SPbU provided computational resources.

REFERENCES

- Alekseev A. 1958. Lamb problem solution for the vertically-inhomogeneous half space (in Russian). *Dynamic Problems of Theory of Elasticity* 6, 167–227.
- Anikiev D., Kazei V., Kashtan B., Ponomarenko A., Troyan V. and Shigapov R. 2014. Methods of seismic waveform inversion. *Seismic Technology* 11(1), 1–32.
- Boiero D., Maraschini M. and Socco L.V. 2009. P and S wave velocity model retrieved by multi modal surface wave analysis. 71st EAGE Conference & Exhibition incorporating SPE EUROPEC, Amsterdam, The Netherlands, Extended Abstracts, T010.
- Boiero D., Wiarda E. and Vermeer P. 2013. Surface and guided-wave inversion for near-surface modeling in land and shallow marine seismic data. *The Leading Edge* 32(6), 638–646.
- Brekhovskikh L.M. 1980. *Waves In Layered Media 2nd Edition (Applied Mathematics and Mechanics, Vol. 16)*. Academic Press.
- Brekhovskikh L.M. and Godin O.A. 1998. *Acoustics of Layered Media I: Plane and Quasi-Plane Waves, Springer Series on Wave Phenomena*. Springer.
- Ernst F.E. 2007. Long-wavelength statics estimation from guided waves. 69th EAGE Conference & Exhibition incorporating SPE EUROPEC, London, U.K., Extended Abstracts, E033.
- Ernst F.E. 2013. Modal elastic inversion. 75th EAGE Conference & Exhibition incorporating SPE EUROPEC, London, U.K., Extended Abstracts, Th 0101.
- Kazei V.V., Troyan V.N., Kashtan B.M. and Mulder W.A. 2013. On the role of reflections, refractions and diving waves in full-waveform inversion. *Geophysical Prospecting* 61(6), 1252–1263.
- Kosloff D., Filho A., Tessmer E. and Behle A. 1989. Numerical solution of the acoustic and elastic wave equations by a new rapid expansion method. *Geophysical Prospecting* 37(4), 383–394.
- Kuvshinov B.N. and Mulder W.A. 2006. The exact solution of the time-harmonic wave equation for a linear velocity profile. *Geophysical Journal International* 167(2), 659–662.
- Maraschini M., Ernst F., Foti S. and Socco L. 2010. A new misfit function for multimodal inversion of surface waves. *Geophysics* 75(4), G31–G43.
- Ponomarenko A.V., Kashtan B.M., Troyan V.N. and Mulder W.A. 2013. Surface wave inversion for a P-wave profile via estimation of the squared slowness gradient. 75th EAGE Conference & Exhibition, London incorporating SPE EUROPEC, U.K., Extended Abstracts, We-P02-10.
- Pratt R.G., Song Z.-M., Williamson P. and Warner M. 1996. Two-dimensional velocity models from wide-angle seismic data by wavefield inversion. *Geophysical Journal International* 124(2), 323–340.
- Ravaut C., Operto S., Imbrota L., Virieux J., Herrero A. and Dell'Aversana P. 2004. Multi-scale imaging of complex structures from multifold wide-aperture seismic data by frequency-domain full-waveform tomography: application to a thrust belt. *Geophysical Journal International* 159(3), 1032–1056.
- Roth M, Holliger K. and Green A.G. 1998. Guided waves in near-surface seismic surveys. *Geophysical Research Letters* 25(7), 1071–1074.

Socco L.V., Foti S. and Boiero D. 2010. Surface-wave analysis for building near-surface velocity models—established approaches and new perspectives. *Geophysics* 75(5), 75A83–75A102.

Tessmer E. 2011. Using the rapid expansion method for accurate time-stepping in modelling and reverse-time migration. *Geophysics* 76(4), S177–S185.

APPENDIX A: DISPERSION EQUATION FOR SINGLE-LAYER MODEL

We present a detailed derivation of the dispersion equation (4). The wave equation (1) for the pressure $P(x, z, t)$ has a velocity model $v_1(z) = v_0/\sqrt{1 - az}$ for $0 \leq z \leq h$ and $v_2(z) = v_1(h)$ for $h \leq z$. The Fourier transform in time and in the horizontal coordinate x is given as

$$P(x, z, t) = \frac{1}{2\pi^2} \operatorname{Re} \int_0^\infty d\omega e^{i\omega t} \int_{-\infty}^\infty dk e^{-ikx} \widehat{P}(k, z, \omega). \quad (\text{A1})$$

This transforms the wave equation (1) into

$$\frac{\partial^2}{\partial z^2} \widehat{P}(k, z, \omega) - \left(k^2 - \frac{\omega^2}{v_1^2(z)} \right) \widehat{P}(k, z, \omega) = 0. \quad (\text{A2})$$

After the change of the coordinates described in Equation (2), equation (A2) reduces to the classic Airy equation (3). This equation has two linearly independent solutions: the two Airy functions $\text{Ai}(\tau)$ and $\text{Bi}(\tau)$ with real argument τ (for example, see Brekhovskikh 1980). Therefore, the analytical expression for the wavefield in the top layer (I) can be expressed as their linear combination. In the half-space (II), it is simply the solution of the wave equation for a homogeneous isotropic medium:

$$P^{\text{I}}(x, z, t) = \frac{1}{2\pi^2} \operatorname{Re} \int_0^\infty d\omega e^{i\omega t} \int_{-\infty}^\infty dk e^{-ikx} \{ A \text{Ai}(\tau) + B \text{Bi}(\tau) \}, \quad (\text{A3})$$

$$P^{\text{II}}(x, z, t) = \frac{1}{2\pi^2} \operatorname{Re} \int_0^\infty d\omega e^{i\omega t} \int_{-\infty}^\infty dk e^{-ikx} C e^{-\alpha_2(z-h)}, \quad (\text{A4})$$

with $\alpha_2 = \sqrt{k^2 - (\omega^2/v_2^2)}$ and functions A , B , and C that do not depend on the spatial coordinates. At the free surface, $P^{\text{I}}|_{z=0} = 0$. Continuity of the pressure and the normal component of the particle velocity at the interface between I and II is prescribed by

$$\begin{aligned} P^{\text{I}} \Big|_{z=h} &= P^{\text{II}} \Big|_{z=h}, \\ \left(\frac{1}{\rho_1} \frac{\partial P^{\text{I}}}{\partial z} \right) \Big|_{z=h} &= \left(\frac{1}{\rho_2} \frac{\partial P^{\text{II}}}{\partial z} \right) \Big|_{z=h}, \end{aligned} \quad (\text{A5})$$

(see Brekhovskikh 1980; Brekhovskikh and Godin 1998). Here, ρ_1 and ρ_2 are the densities in the layer and in the half-space. We only consider a continuous constant-density

medium, so $\rho_1|_{z=h} = \rho_2|_{z=h}$. Together with (A3) and (A4), we obtain the system of equations

$$\begin{cases} \{ A \text{Ai}(\tau) + B \text{Bi}(\tau) \} |_{z=0} = 0, \\ \{ A \text{Ai}(\tau) + B \text{Bi}(\tau) \} |_{z=h} = C, \\ \frac{\partial}{\partial z} \{ A \text{Ai}(\tau) + B \text{Bi}(\tau) \} |_{z=h} = -\alpha_2 C. \end{cases} \quad (\text{A6})$$

Using $\frac{\partial f}{\partial z} = \frac{\partial f}{\partial \tau} \frac{\partial \tau}{\partial z} = H^{-1} \frac{\partial f}{\partial \tau}$, we obtain the dispersion equation as the solvability condition of the system (A6):

$$\begin{aligned} \mathcal{D}(k, \omega) &= \text{Ai}(\tau)|_{z=0} \{ \text{Bi}'(\tau)|_{z=h} + H\alpha_2 \text{Bi}(\tau)|_{z=h} \} \\ &\quad - \text{Bi}(\tau)|_{z=0} \{ \text{Ai}'(\tau)|_{z=h} + H\alpha_2 \text{Ai}(\tau)|_{z=h} \} = 0, \end{aligned} \quad (\text{A7})$$

where the primes denote the derivatives with respect to τ . Recall that $\tau = \tau_0 + (z/H)$, $\tau_0 = H^2(k^2 - k_0^2)$, $k_0 = \omega/v_0$, $H = (ak_0^2)^{-1/3}$, $\alpha_2 = \sqrt{k^2 - (\omega/v_2)^2}$, and $v_2 = v_0/\sqrt{1 - ah}$ for model parameters v_0 , a , and h .

APPENDIX B: DISPERSION EQUATION FOR A TWO-LAYER MODEL

We also present the dispersion equation for two layers above a half-space. The velocity in the first layer is $v_1(z) = v_0/\sqrt{1 - a_1z}$ for $0 \leq z \leq h_1$, and that in the second layer is $v_2(z) = v_0/(\sqrt{1 - a_1h_1}\sqrt{1 - a_2(z - h_1)})$ for $h_1 \leq z \leq h_2$. The halfspace has $v_3 = v_2(h_2)$ for $z \geq h_2$. There are no velocity contrasts, and the density is constant for the whole model.

Similar to the single-layer model, the pressures in the two layers (I, II) and in the half-space (III) can be expressed as

$$P^{\text{I}} = A \text{Ai}(\tau_1) + B \text{Bi}(\tau_1), \quad (\text{B1})$$

$$P^{\text{II}} = C \text{Ai}(\tau_2) + D \text{Bi}(\tau_2), \quad (\text{B2})$$

$$P^{\text{III}} = E e^{-\alpha_3(z-h_2)}, \quad (\text{B3})$$

with $\alpha_3 = \sqrt{k^2 - (\omega^2/v_3^2)}$, $\tau_1 = \tau_{01} + z/H_1$, $\tau_{01} = H_1^2(k^2 - k_{01}^2)$, $H_1 = (a_1k_{01}^2)^{-1/3}$, $k_{01} = \omega/v_0$, $\tau_2 = \tau_{02} + (z - h_1)/H_2$, $\tau_{02} = H_2^2(k^2 - k_{02}^2)$, $H_2 = (a_2k_{02}^2)^{-1/3}$, $k_{02} = \omega/v_2(h_1)$, and functions A , B , C , D , and E that do not depend on the spatial coordinates.

At the free surface, $P^{\text{I}}|_{z=0} = 0$. Continuity of the pressure and the normal component of the particle velocity at the two interfaces is prescribed by

$$\begin{aligned} P^{\text{I}} \Big|_{z=h_1} &= P^{\text{II}} \Big|_{z=h_1}, \\ \left(\frac{1}{\rho_1} \frac{\partial P^{\text{I}}}{\partial z} \right) \Big|_{z=h_1} &= \left(\frac{1}{\rho_2} \frac{\partial P^{\text{II}}}{\partial z} \right) \Big|_{z=h_1}, \end{aligned} \quad (\text{B4})$$

$$\begin{aligned}
 p^{\text{II}} \Big|_{z=h_2} &= p^{\text{III}} \Big|_{z=h_2}, \\
 \left(\frac{1}{\rho_2} \frac{\partial p^{\text{II}}}{\partial z} \right) \Big|_{z=h_2} &= \left(\frac{1}{\rho_3} \frac{\partial p^{\text{III}}}{\partial z} \right) \Big|_{z=h_2},
 \end{aligned} \tag{B5}$$

where ρ_1 , ρ_2 , and ρ_3 are the densities of the first layer, second layer, and half-space, respectively. Here, they are replaced by a single constant density. Together with (B1), (B2), and (B3), we obtain the system of equations:

$$\left\{ \begin{aligned}
 &\{AAi(\tau_1) + BBi(\tau_1)\}|_{z=0} = 0, \\
 &\{AAi(\tau_1) + BBi(\tau_1)\}|_{z=b_1} \\
 &\quad = \{CAi(\tau_2) + DBi(\tau_2)\}|_{z=b_1}, \\
 &\{AAi'(\tau_1) + BBi'(\tau_1)\}|_{z=b_1} \\
 &\quad = \left\{ \frac{H_1}{H_2} (CAi'(\tau_2) + DBi'(\tau_2)) \right\} \Big|_{z=b_1}, \\
 &\{CAi(\tau_2) + DBi(\tau_2)\}|_{z=h_2} = E, \\
 &\{CAi'(\tau_2) + DBi'(\tau_2)\}|_{z=h_2} = -\alpha_3 H_2 E.
 \end{aligned} \right. \tag{B6}$$

Here the primes denote the derivatives with respect to the argument in brackets.

The dispersion equation is again obtained as the solvability condition of the system (B6). This can be written as the following determinant, with $\tau_1|_{z=0} = \tau_{01}$, $\tau_2|_{z=b_1} = \tau_{02}$, and $T_1 = \tau_1|_{z=b_1}$ with $T_2 = \tau_2|_{z=h_2}$:

$$\begin{vmatrix}
 Ai(\tau_{01}) & Bi(\tau_{01}) & 0 & 0 & 0 \\
 Ai(T_1) & Bi(T_1) & -Ai(\tau_{02}) & -Bi(\tau_{02}) & 0 \\
 Ai'(T_1) & Bi'(T_1) & -\frac{H_1}{H_2} Ai'(\tau_{02}) & -\frac{H_1}{H_2} Bi'(\tau_{02}) & 0 \\
 0 & 0 & Ai(T_2) & Bi(T_2) & -1 \\
 0 & 0 & Ai'(T_2) & Bi'(T_2) & \alpha_3 H_2
 \end{vmatrix} = 0. \tag{B7}$$

After evaluation, (B7) leads to the dispersion equation:

$$\begin{aligned}
 \mathcal{D}(k, \omega) &= (Ai(\tau_{01}) Bi'(T_1) - Ai'(T_1) Bi(\tau_{01})) \\
 &\quad [H_2 \alpha_3 (Ai(\tau_{02}) Bi(T_2) - Ai(T_2) Bi(\tau_{02})) \\
 &\quad + (Ai(\tau_{02}) Bi'(T_2) - Ai'(T_2) Bi(\tau_{02}))] \\
 &\quad - \frac{H_1}{H_2} (Ai(\tau_{01}) Bi(T_1) - Ai(T_1) Bi(\tau_{01})) \\
 &\quad [H_2 \alpha_3 (Ai'(\tau_{02}) Bi(T_2) - Ai(T_2) Bi'(\tau_{02})) \\
 &\quad + (Ai'(\tau_{02}) Bi'(T_2) - Ai'(T_2) Bi'(\tau_{02}))] = 0.
 \end{aligned} \tag{B8}$$